Nano Research

Open Access

Research Article

Digital immunoassay of interleukin-6 by plasmonic coupling of SERS nanotags with gold-capped micropillar array

Qifan Zhou[1,2,§], Miaomiao Li[3,§], Chaima Merzougui[1,2], Yu Lu[1,2], Jun Sun[1,2], Chuang Qi[1], Yan Huang[1,2], Cheng Chen[4], Jinliang Sheng[3], Hui Zhang[3] ✉, Xiaoyi Lv[4] ✉, and Xiangwei Zhao[1,2,3] ✉

[1] *State Key Laboratory of Digital Medical Engineering, School of Biological Science and Medical Engineering, Southeast University, Nanjing 211189, China*
[2] *Southeast University Shenzhen Research Institute, Shenzhen 518000, China*
[3] *State International Joint Research Center for Animal Health Breeding, College of Animal Science and Technology, Shihezi University, Shihezi 832003, China*
[4] *College of Software, Xinjiang University, Urumqi 830046, China*
§ *Qifan Zhou and Miaomiao Li contributed equally to this work.*

Cite this article: *Nano Research*, **2027**, *20*, 94909231. https://doi.org/10.26599/NR.2026.94909231

ABSTRACT: Digital immunoassays hold great potential for the ultra-sensitive detection of low-abundance biomarkers. In this research, a high-performance digital immunoassay platform by plasmonic coupling of surface-enhanced Raman scattering (SERS) nanotags with gold-capped micropillar array was developed. Ultraviolet lithography (UVL) was implemented for the cost-effective, wafer-scale fabrication of highly ordered gold-capped micropillar arrays with tunable dimensions. By combining high-activity Au@Ag-Au SERS nanotags, a classic particle-on-mirror (PoM) coupling effect was realized on the chip for effective Raman signal amplification. Furthermore, a dual-mode strategy combining spatial digital counting and Raman peak intensity was adopted to overcome the dynamic range limitations and potential signal distortions common in conventional digital readouts. As a proof-of-concept, the proposed platform demonstrated favorable analytical performance of interleukin-6 (IL-6) detection, exhibiting a linear dynamic range from 100 fg/mL to 1 ng/mL and a limit of detection (LOD) of 16.9 fg/mL. This platform successfully bridges reliable, low-cost plasmonic nanostructure design with high-precision signal processing, paving the way for scalable and precise digital bioassays.

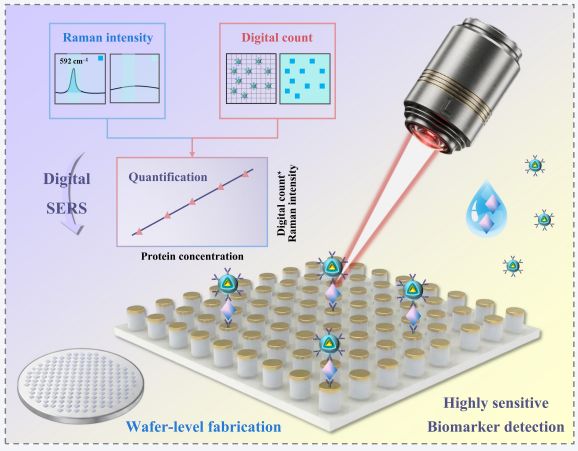

KEYWORDS: digital immunoassay, plasmonic coupling, biomarker detection, micropillar array, interleukin-6 (IL-6)

1 Introduction

Ultrasensitive immunoassay of protein biomarkers plays an indispensable role in the early screening, precise staging, and prognostic assessment of disease [1]. Traditional immunoassays (e.g., enzyme-linked immunosorbent assay (ELISA)) frequently encounter bottlenecks, including limited sensitivity, cumbersome operational procedures, and insufficient multiplexing capabilities [2, 3]. Surface-enhanced Raman scattering (SERS) has emerged as a highly promising technique for the trace detection of biomarkers, owing to its unique molecular fingerprinting, single-molecule-level sensitivity, and excellent resistance to photobleaching [4, 5]. However, conventional SERS quantitative methods based on analog signal intensity face formidable challenges in ultra-low concentration detection. Because SERS signals are highly dependent on the distribution of plasmonic "hot spots" [6], minute structural inhomogeneities on the substrate surface and the random distribution of target molecules within these regions inevitably lead to dramatic signal fluctuations [7]. Such poor signal reproducibility significantly compromises the accuracy and reliability of SERS in the quantitative analysis of trace targets.

To overcome the inherent limitations of conventional analog SERS, digital SERS has emerged as a transformative approach

Received: July 24, 2026; **Revised:** September 3, 2026
Accepted: September 30, 2026

✉Address correspondence to Hui Zhang, prof.zhang@foxmail.com; Xiaoyi Lv, lvxiaoyi@xju.edu.cn; Xiangwei Zhao, xwzhao@seu.edu.cn

[8–11]. The core principle of this technology involves converting continuous and highly fluctuating analog signals into discrete, countable digital signals ("0" or "1"). Quantification is thereby achieved by counting the number of "active units" containing the target molecules [12, 13]. By relying on single-molecule counting, this strategy fundamentally mitigates the impact of signal fluctuations caused by the heterogeneous distribution of hot spots, significantly improving quantitative accuracy at ultra-low concentrations. Within current digital SERS research, label-free modes are often constrained by the extremely small Raman scattering cross-sections of biomacromolecules [14–16]. In contrast, label-based digital detection utilizing SERS nanotags provides stable, intense characteristic signals and has thus become the mainstream approach for achieving high-sensitivity detection [17].

The prerequisite for high-fidelity digital SERS detection lies in the effective spatial isolation of individual target molecules. Currently, spatial isolation is primarily achieved through two distinct strategies: virtual discretization and physical compartmentalization [18]. Virtual discretization typically relies on large-area scanning of planar substrates using high-resolution confocal Raman microscopy [19, 20]. However, this method is highly susceptible to focal spot drift and overlapping signal sampling, making ideal single-molecule counting difficult to attain. In contrast, spatially ordered microstructural arrays fabricated via micro/nanofabrication techniques enable more efficient physical compartmentalization. From a structural design perspective, micropillar arrays exhibit superior washing efficiency and spatial accessibility compared to conventional microwell arrays [21]. This topological design significantly mitigates steric hindrance and enhances the binding probability of target molecules during the immunoassay, thereby endowing the detection system with a higher signal-to-noise ratio (SNR). Nevertheless, most existing micropillar array substrates rely on high-precision fabrication techniques, such as electron beam lithography (EBL) [22–24], focused ion beam (FIB) milling [25], or femtosecond laser direct writing (FsLDW) [26]. These methods suffer from inherent drawbacks, including exorbitant costs, complex procedures, and difficulties in ensuring wafer-scale batch-to-batch consistency. By comparison, ultraviolet lithography (UVL) offers outstanding capabilities for wafer-scale, large-area patterning along with exceptionally high throughput [27]. UVL can significantly reduce manufacturing costs while guaranteeing the strict periodicity and batch-to-batch consistency of micro structured arrays [28, 29], thereby serving as a highly promising, scalable alternative for physical compartmentalization. Furthermore, in terms of data processing, existing digital SERS analyses are largely confined to a simplistic binarized spatial counting mode [30–33]. Although this approach mitigates background interference, it entirely discards the rich Raman spectral intensity information intrinsic to the immunocomplexes, ultimately restricting the dynamic range and ultimate precision of target quantification.

To systematically address these challenges, this research develops a cost-effective, wafer-scale digital SERS immunoassay platform based on standard UVL technology. Compared to conventional expensive micro/nanofabrication techniques, the UVL strategy ensures high precision and consistency of the micropillar arrays while facilitating high-throughput processing, thereby laying a practical foundation for the mass production of sensing chips. For the detection system, we utilize core–shell Au@Ag-Au nanotags with single-particle Raman activity that form a particle-on-film gap-mode plasmonic coupling with the gold-capped micropillars, achieving signal amplification. For data processing, the original Raman spectral mappings were converted into binary mask images via a statistical thresholding method and subsequently convolved with the raw intensity images. This approach enables the precise extraction of both the rate of positive pixels (RPP) and the corresponding average Raman intensity (ARI). By integrating spatial digital counting with spectral intensity (RPP × ARI), this dual-dimensional metric effectively mitigates the information loss and signal saturation issues inherent in traditional methods. As a proof-of-concept, the platform was applied to the quantitative analysis of interleukin-6 (IL-6), achieving a limit of detection (LOD) of 16.9 fg/mL and a broad linear dynamic range from 100 fg/mL to 1 ng/mL. Ultimately, this research not only provides a scalable engineering strategy for manufacturing high-throughput SERS sensing interfaces but also establishes a reliable methodological framework for the accurate detection of low-abundance protein biomarkers.

2 Experiment section

2.1 Fabrication process of microarray chip

First, a 4-inch single-side polished silicon wafer was selected as the substrate. To thoroughly remove surface organic contaminants, the wafer was sequentially rinsed with acetone, ethanol, and deionized (DI) water, followed by drying with high-purity nitrogen (N_2) gas. Subsequently, an oxygen plasma treatment was performed at a power of 400 W for 5 min to further enhance surface cleanliness. To improve the adhesion between the photoresist and the substrate, the wafer was placed in a hexamethyldisilazane (HMDS) pretreatment system for 10 min, rendering the substrate hydrophobic and oleophilic through surface chemical modification. During the pattern definition stage, an AZ 5214 positive photoresist was spin-coated onto the silicon wafer at a rotation speed of 4000 rpm using a manual spin coater, controlling the resist thickness to approximately 1.5 μm. The wafer was then soft-baked on a hotplate at 95 °C for 90 s to evaporate the solvent and solidify the resist film. The exposure process was conducted using a SUSS MA6 UV aligner with a precise exposure time of 7 s, followed by immersion in a 2.38% tetramethylammonium hydroxide (TMAH) developer for 45 s. After rinsing with DI water and nitrogen drying, the array patterns on the photomask were successfully transferred onto the silicon surface, achieving high-quality photolithographic pattern definition. Afterward, a 10 nm thick Cr adhesion layer and a 150 nm thick Au film were sequentially deposited on the patterned silicon wafer using an EI-5Z electron-beam evaporation system. Following deposition, the sample was immersed in an acetone solution for approximately 12 h to fully dissolve the photoresist, assisted by ultrasonic agitation in acetone and isopropanol for 5 min each, thereby obtaining the metallic array patterns via a lift-off process. Using this metal layer as a hard mask, anisotropic plasma etching was performed utilizing a surface technology systems advanced silicon etching high rate module (STS-ASE HRM) deep reactive ion etching (DRIE) system, ultimately constructing gold-capped micropillar arrays with a height of 1.2 μm. At the final stage of the fabrication process, the wafer was diced into individual 5 mm × 5 mm sensing units using a DISCO precision dicing saw.

2.2 Chemical modification of microarray chip

First, the chips were sequentially rinsed with acetone, ethanol, and

DI water. Following nitrogen drying, the chips were immersed in a 10 mM 11-MUA ethanol solution and incubated at 4 °C in the dark for 24 h to form a carboxylated self-assembled monolayer (SAM) on the gold-capped surfaces via Au–S bonding. Subsequently, ethanol and DI water were alternately used to rinse the chips to eliminate physically adsorbed impurities. The surface carboxyl groups were activated *in situ* for 30 min using an EDC/NHS coupling system (200 mM/50 mM in 0.1 M MES buffer, pH = 5.5). Immediately after activation, the chips were washed with PBS, and an IL-6 capture antibody solution (50 μg/mL) was promptly introduced for overnight incubation at 4 °C, achieving oriented antibody immobilization through covalent coupling. Finally, a 2% bovine serum albumin (BSA) solution (containing 0.05% Tween20) was employed to block nonspecific binding sites at 37 °C for 1 h. The functionalized chips were stored at 4 °C for future use.

2.3 Sensitive detection of IL-6 on microarray chip

First, standard IL-6 antigen solutions were serially diluted with PBS buffer to yield a concentration gradient ranging from 100 fg/mL to 1 ng/mL. Then, 100 μL of the prepared antigen solution was introduced onto the functionalized gold-capped micropillar array chip and incubated at 37 °C for 90 min, facilitating the specific capture of IL-6 via antigen-antibody affinity interactions. Following the incubation, the chip was rinsed three times with a phosphate buffered saline (PBS) washing buffer (containing 0.1% BSA and 0.01% Tween 20) to remove unbound biomolecules and nonspecifically adsorbed impurities. Subsequently, 100 μL of the antibody-conjugated SERS nanotags (synthesis strategy was shown in Section S2 in the Electronic Supplementary Material (ESM)) was dispensed onto the chip surface and incubated at 37 °C for an additional 30 min. After washing, the chip was dried and stored at 4 °C prior to Raman signal acquisition.

2.4 SERS measurement and data analysis

SERS spectra from the chip surface were acquired using a Renishaw InVia Raman microscope (Renishaw, UK). Prior to the measurements, the optical system was calibrated using the characteristic peak of a single-crystal silicon wafer at 520.5 cm^{-1}. Spectral measurements were performed using a 633 nm excitation laser at a power of 0.3 mW, which was focused through a 100× objective lens (NA = 0.85). A random sampling strategy was applied to the micropillar arrays on the chip surface. Three independent 10 × 10 micropillar grids were subjected to Raman mapping, with an exposure time of 1 s per point.

The raw SERS spectra were processed for baseline correction and fluorescence background subtraction using Renishaw WiRE 4.2 software. Data analysis focused on the characteristic Raman peak of NBA at 592 cm^{-1}. A custom Python script was utilized for the automated processing of the spectral data to extract the peak intensities at 592 cm^{-1}. Finally, statistical analysis, standard curve regression fitting, and graphical plotting were performed using Origin Pro 2022 software.

3 Results and discussion

3.1 Principle of digital SERS detection based on gold-capped micropillar array

As illustrated in Fig. 1, this research proposes a digital SERS detection strategy for protein biomarkers based on a wafer-scale gold-capped micropillar array. Utilizing high-precision and cost-effective UVL, we enabled a large-scale preparation of micro-sized, highly consistent ordered arrays. The platform capitalizes on topographic physical isolation and the distinct material properties of the "gold cap versus silicon bottom" to achieve spatially selective chemical modification. This ensures that capture antibodies are strictly anchored to the tops of the individual micropillars, fundamentally suppressing non-specific background noise. Following a typical sandwich immunoassay, biomarker capture events on the pillar tops translate molecular concentration into localized SERS signals. At ultralow target concentrations, the spatial distribution of these capture events adheres to a Poisson distribution, successfully transitioning the readout from a conventional continuous bulk analog signal to discrete single-molecule counts. Detection signal is further amplified by the particle-on-mirror (PoM) plasmonic coupling effect generated between the underlying gold film and the captured SERS nanotags. For signal analysis, this research circumvents the limitations of conventional binary digital readouts by introducing a composite metric, RPP × ARI. This metric integrates the rate of positive pixels

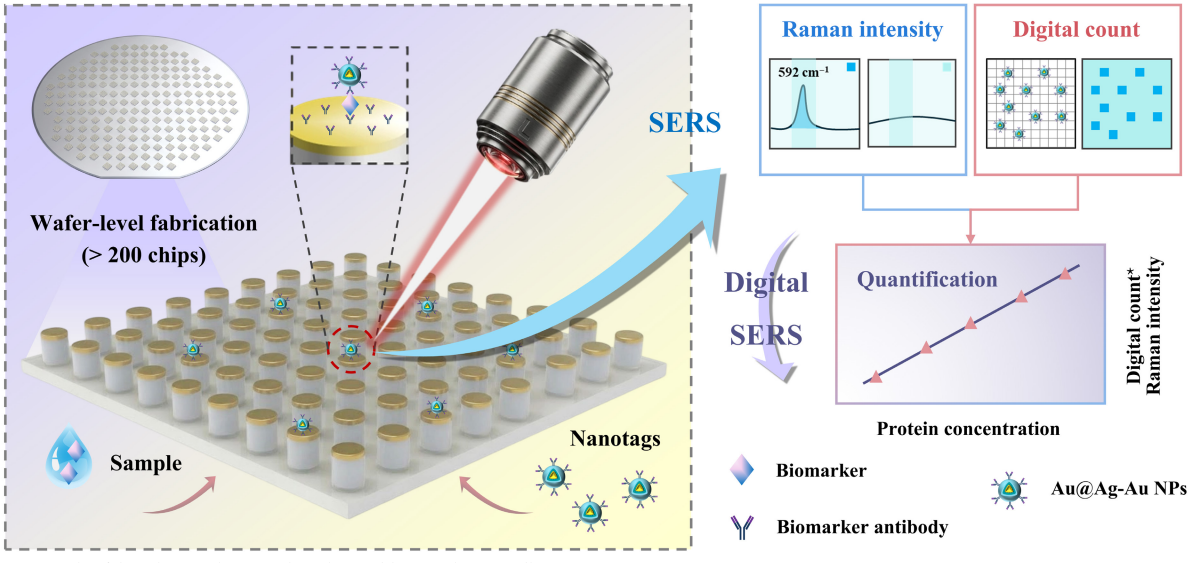

Figure 1 Principle of digital SERS detection based on gold-capped micropillar array.

(RPP, representing the spatial distribution frequency of the signals) with the average Raman intensity (ARI, denoting the optical signal gain of individual monomers). By integrating the statistical information from discrete digital events with the Raman intensity information of positive regions, this dual-mode strategy mitigates signal fluctuations while maintaining high sensitivity and measurement reliability (the theoretical basis is provided in Section S5 in the ESM). Consequently, it enables accurate quantification of low-abundance protein biomarkers over a broad dynamic range.

3.2 Characterization of gold-capped micropillar array chip

Digital SERS analysis governed by Poisson statistics requires substrates with highly uniform nanotags binding probabilities and the capacity for interference-free spectral acquisition. To address this, a manufacturing strategy integrating UVL with thin-film deposition was developed. By combining lithographic patterning, Cr/Au layer deposition, and deep silicon etching, wafer-scale gold-capped micropillar arrays were successfully fabricated on silicon substrates (Figs. 2(a) and 2(b)). As shown in Fig. 2(c), approximately 210,000 (460 × 460) independent micropillars, each 1.2 μm in height, 5 μm in diameter, and spaced 10 μm apart, are uniformly distributed within a 5 mm × 5 mm sensing unit. This geometric configuration strikes an optimal balance between effective surface area and spatial resolution. It maximizes antibody loading capacity while utilizing the 10 μm spacing to prevent spectral overlap between adjacent signals, perfectly satisfying the physical spatial segmentation required for digital sampling (Fig. 2(d)). Compared to expensive and time-consuming EBL or FIB techniques, this UVL process significantly reduces fabrication costs while maintaining excellent patterning precision and morphological tunability, demonstrating immense potential for large-scale, high-throughput industrial production.

To spatially localize the detection regions, highly selective surface modification was performed on the gold caps of the micropillars

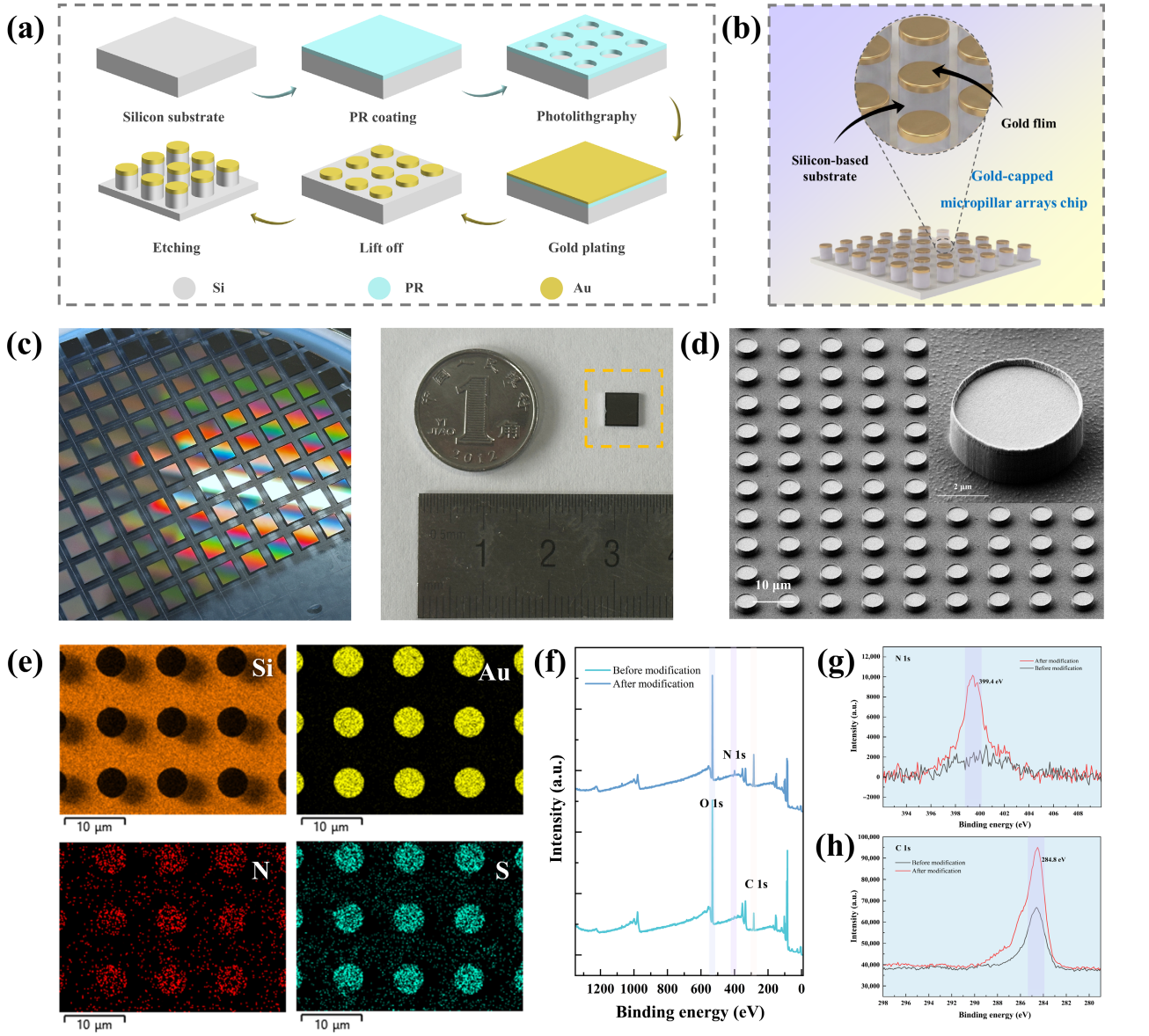

Figure 2 (a) Schematic illustration of the chip fabrication process. (b) Schematic diagram of the chip structure. (c) Optical photograph of the fabricated chip. (d) SEM image of the micropillar array. (e) EDS elemental mapping images of the modified chip. (f) Comparison of XPS survey spectra before and after modification. Comparison of high-resolution XPS spectra for (g) N 1s and (h) C 1s.

using 11-MUA self-assembly combined with EDC/NHS coupling chemistry (Fig. S1 in the ESM). This protocol leverages the strong chemical affinity of Au–S bonds to construct a carboxylated interface on the gold surface. This interface is subsequently converted into a highly reactive NHS ester intermediate, allowing for the covalent immobilization of capture antibodies via a nucleophilic substitution reaction. Benefiting from the chemical inertness of the exposed silicon substrate towards thiol molecules, this strategy ensures that the capture antibodies are strictly and specifically confined to the gold caps. This fundamental elimination of non-specific binding in non-detection areas provides dual physical and chemical guarantees for subsequent digital counting.

The spatially selective modification was further validated using energy dispersive spectroscopy (EDS) and X-ray photoelectron spectroscopy (XPS) characterizations. Scanning electron microscope (SEM) and EDS analyses confirmed that the chemical modification process did not damage the micropillar morphology (Fig. 2(e) and Fig. S2 in the ESM). Notably, the spatial distribution of Au, S and N elemental signals highly overlapped and were precisely localized at the micropillar caps. This visual evidence confirms the specific self-assembly of the 11-MUA monolayer and the precise immobilization of antibodies, effectively ruling out non-specific adsorption on the silicon substrate. Furthermore, the XPS survey spectrum (Fig. 2(f)) revealed a distinct N signal and an enhanced C signal following modification. In the high-resolution spectra, the emergence of the N 1s peak (Fig. 2(g)) and the formation of a broad shoulder corresponding to amide bonds in the C 1s spectrum (Fig. 2(h)) conclusively verified the successful covalent conjugation of the capture antibodies onto the gold caps at the chemical bond level. Collectively, these results demonstrate that stable and highly selective functionalization has been achieved in the designated sensing regions of the chip, perfectly fulfilling the experimental prerequisites for digital SERS detection.

3.3 Characterization of SERS nanotags

The synthesis of the SERS nanotags followed our previously established seed-mediated growth and galvanic replacement strategy (Section S2 and Fig. S3 in the ESM) [34, 35]. The morphological evolution of the nanoparticles at each synthesis stage is illustrated in Figs. 3(a)–3(c), ultimately yielding Au-core/Au-Ag alloy-shell (Au@Ag-Au) nanoparticles that serve as the core SERS signal amplification elements. To address the issue of trace rod-like byproducts in the final products, which may compromise single-particle signal uniformity during digital detection, a depletion-force-

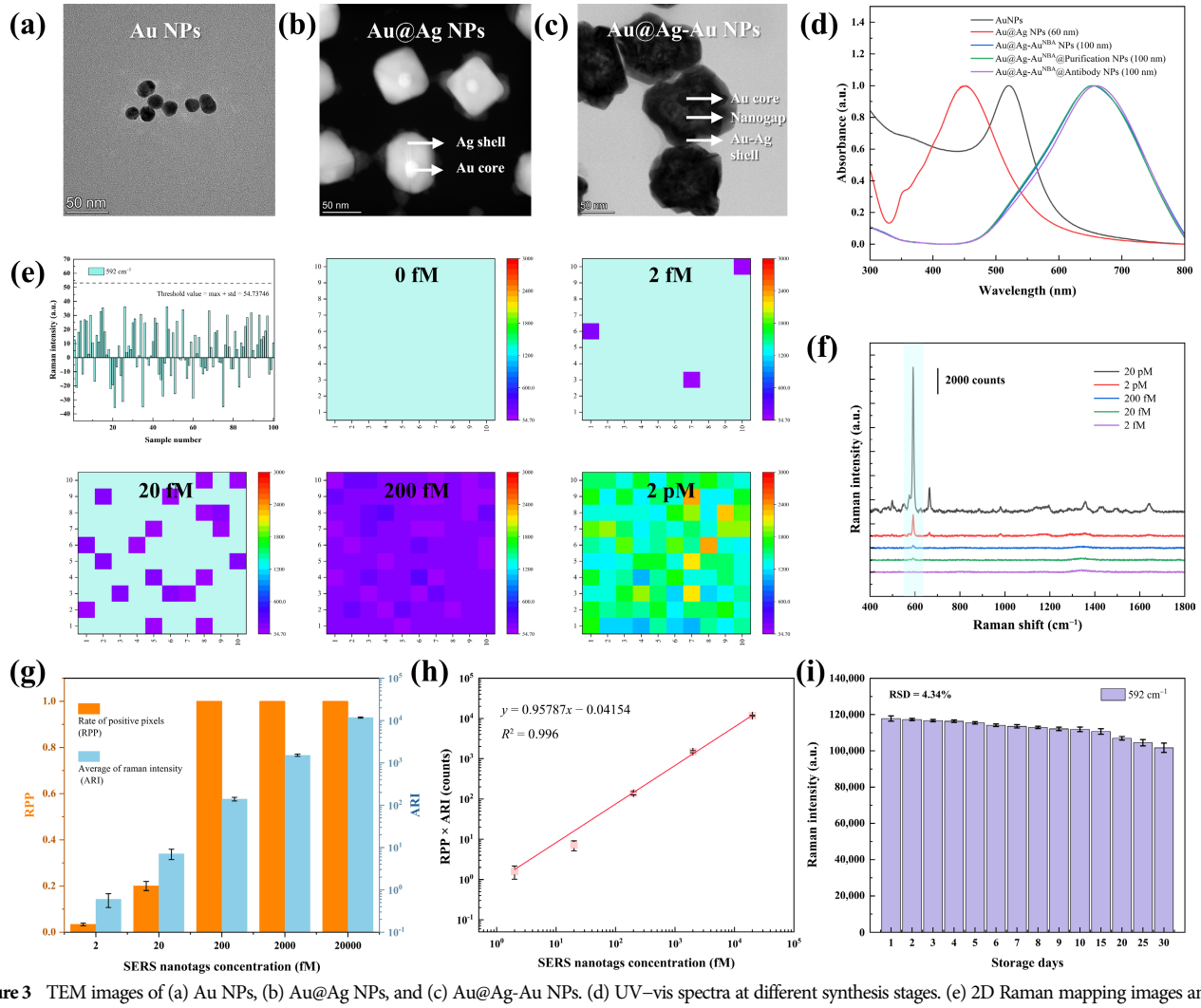

Figure 3 TEM images of (a) Au NPs, (b) Au@Ag NPs, and (c) Au@Ag-Au NPs. (d) UV–vis spectra at different synthesis stages. (e) 2D Raman mapping images and (f) representative Raman spectra of the nanotag solutions at various concentrations. (g) RPP and ARI of the positive regions, and (h) the corresponding calibration curve across different concentrations. (i) Storage stability of the SERS nanotags.

induced gravity-driven deposition method was employed for purification (Fig. S4 in the ESM) [36]. Ultraviolet–visible (UV–Vis) spectroscopy was utilized to continuously monitor the LSPR evolution throughout the Au@Ag-Au synthesis process (Fig. 3(d)). During the core–shell construction stage, owing to the controlled epitaxial growth of the Ag shell onto the Au cores, the LSPR peak of the 60 nm Au@Ag NPs blue-shifted from that of the pure Au cores (520 nm) and stabilized at 452.5 nm. Upon entering the galvanic replacement and growth stage, the compositional transition of the shell from pure Ag to an Au-Ag alloy caused a substantial red-shift of the resonance peak to 652.5 nm. Following depletion-force purification to remove anisotropic byproducts, the peak exhibited a slight red-shift and stabilized at 654.4 nm. After specific bioconjugation, the peak further red-shifted to 659.5 nm due to the increased local refractive index induced by the antibody molecular layer. This continuous optical shift experimentally corroborated the successful loading of antibodies. Comparative SERS activity analysis across different stages (Fig. S5 in the ESM) demonstrated that the Au@Ag-Au nanostructures exhibited an excellent electromagnetic enhancement effect, with a calculated enhancement factor (EF) of 3.47×10^5 (Section S6 and Fig. S6 in the ESM). Furthermore, the bioconjugation process did not cause a noticeable attenuation in SERS intensity. This indicates that the nanotags possess exceptional optical robustness and can effectively preserve the "hot spot" intensity on the metal surface, making them highly suitable for complex immunoassay environments.

Addressing the stringent requirements of digital SERS detection for single-particle activity, we systematically evaluated the single-particle SERS response of the nanotags in aqueous solutions. Two-dimensional Raman mapping images were acquired over a broad concentration range from 2 fM to 20 pM. To accurately extract single-particle signals from complex environmental backgrounds, a rigorous statistical threshold was established, defined as the sum of the maximum background intensity of a blank sample and its standard deviation, based upon which pseudo-color images were generated (Fig. 3(e)). Representative Raman spectra at various concentrations (Fig. 3(f)) clearly illustrate the variation trend of characteristic peak intensities with respect to particle density. To comprehensively quantify this concentration dependence, two evaluation metrics (RPP and ARI) were introduced. As shown in Fig. 3(g), in the ultralow concentration regime (2 to 200 fM), RPP decreased significantly as the concentration lowered due to the sparse distribution of particles within the sampling area; meanwhile, ARI reflected the average signal gain of single particles within the detected regions. To comprehensively integrate the particle distribution frequency and the monomer enhancement intensity, a composite metric, RPP × ARI, was employed for quantitative correlation analysis. The results (Fig. 3(h)) revealed that this composite metric exhibited an excellent linear relationship (R^2 = 0.996) over a wide concentration range, fully confirming the highly reliable single-particle activity and signal yield of the nanotags. Additionally, a 30-day storage stability test of the nanotags demonstrated a relative standard deviation (RSD) of only 4.34% in characteristic signal intensity (Fig. 3(i)), proving that the nanotags retain stable physicochemical properties after long-term storage, meeting the practical demands of biosensing applications.

3.4 Performance of SERS detection on Chip

To evaluate the specific recognition performance of the gold-capped micropillar array chip (Fig. 4(a)), micro-morphological and spectroscopic analyses were initially performed. SEM imagery demonstrated that the target antigen in the positive group successfully mediated the specific capture of SERS nanotags on the gold-capped surface (Fig. 4(b)), whereas no obvious non-specific adsorption was observed in the negative control group (Fig. 4(c)). Subsequent confocal Raman spectroscopic analysis revealed that the characteristic peak derived from the silicon substrate at 520 cm^{-1} completely vanished in the positive group (Fig. 4(d)). This confirms that the spatial geometric isolation of the "gold cap/silicon base" configuration, coupled with confocal axial planar focusing, effectively shields the background interference from the underlying silicon wafer, thereby significantly improving the SNR. Aside from the background suppression, the outstanding SNR is also closely governed by the signal amplification at the interface. Finite-difference time-domain (FDTD) simulations were performed to systematically investigate the electromagnetic field distribution at the interactive interface between the nanoparticles and the substrate (Section S7 in the ESM). The results indicated that upon capture of the nanotags onto the gold-capped surface under 633 nm laser excitation, a strong image dipole interaction occurs between the nanoparticles and the underlying gold film, triggering the classic PoM coupling effect. This strong plasmonic coupling strongly compresses the optical energy into the vertical nanogaps and the internal cavities of the particles, thereby constructing highly localized "hotspots" with significantly amplified electromagnetic field intensity (Fig. 4(e)). In contrast, on a conventional Si substrate, the electromagnetic field enhancement is profoundly deficient due to the lack of free electrons in semiconductor materials to support LSPR (Fig. 4(f)). Transverse line-profile electric field distribution curves further revealed that the localized field induced by the gold-film substrate not only exhibits a higher peak intensity but also displays a narrower full width at half maximum, demonstrating pronounced spatial localization characteristics (Fig. 4(g)). This theoretical expectation was strongly validated by Raman intensity comparison experiments (Fig. 4(h) and Section S8 in the ESM), where the intensity of the characteristic Raman peak (592 cm^{-1}) on the gold-capped micropillar array was enhanced by 177.97% compared to that on the Si substrate group. The synergistic effect of this background suppression and the PoM plasmonic coupling enhancement constitutes the core physical foundation for the high-sensitive detection of the chip. The slightly higher experimental enhancement (1.77-fold) than the simulated value (1.42-fold) may originate from nanoscale roughness and local morphological variations of the fabricated Au surface, which can introduce additional localized field enhancement beyond the idealized FDTD model. To convert the aforementioned high-SNR spectral matrix into discrete digital counting signals, a digital identification threshold was established based on the residual intensity fluctuations of the negative blank background at 592 cm^{-1} using the standard 3σ rule (mean plus three times the standard deviation) (Fig. 4(i)). Guided by this threshold logic, the raw Raman imaging data were converted into a binarized digital matrix (Fig. 4(j)): Pixels above the threshold were defined as valid digital signals generated by specific binding (assigned a value of "1"), presenting distinct NBA characteristic fingerprint peaks; conversely, areas below the threshold were categorized as systemic background noise (assigned a value of "0"), manifesting as flat baselines. The results confirm that this adaptive binarization threshold standard can efficiently filter out instrumental perturbations and random noise, laying a solid data foundation for highly sensitive and robust digital SERS detection.

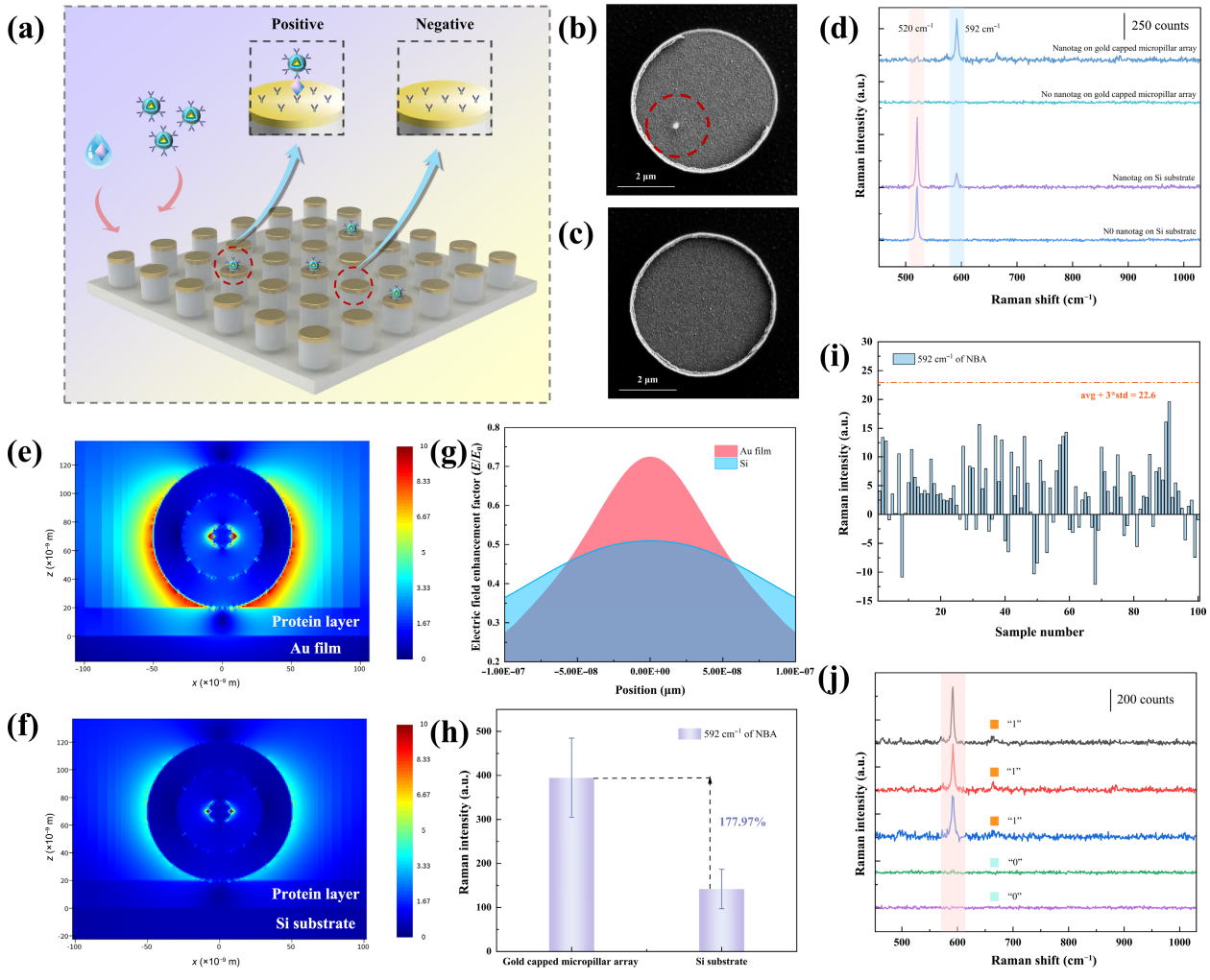

Figure 4 (a) Schematic of the positive and negative assays. SEM images of the gold surfaces after incubation with the (b) positive sample and (c) negative control. (d) Representative Raman spectra obtained from different substrates. (e) FDTD simulation of the electromagnetic field distribution at the interactive interface between the nanotag and the gold film substrate. (f) FDTD simulation of the electromagnetic field distribution at the interactive interface between the nanotag and the Si substrate. (g) Transverse line-profiles of the localized electric field distributions on different substrates. (h) Comparison of the SERS signal intensities among different substrates. (i) Statistical distribution of Raman intensities at 592 cm^{-1} from 100 negative regions. The orange dashed line indicates the calculated threshold. (j) Representative Raman spectra of the positive and negative regions.

3.5 Optimization of experimental parameters

To maximally suppress non-specific adsorption and enhance the accuracy of digital counting, the surface blocking system of the chip was first optimized. Solutions of 2% BSA, casein, and non-fat milk were independently evaluated as blocking agents (incubated at 37 °C for 1 h). As shown in Fig. 5(a), when testing a 1 ng/mL IL-6 positive sample, all three groups achieved a RPP approaching 100%. However, in the negative control assays, the background RPP for the casein and non-fat milk groups increased significantly. In contrast, owing to its optimal molecular size, BSA can construct a denser steric hindrance and physical barrier on the quasi-planar gold-capped micropillars, effectively preventing the non-specific binding of interfering proteins. Accordingly, 2% BSA was selected as the optimal blocking agent.

The incubation duration of the SERS nanotags directly dictates the formation efficiency of the immunocomplexes and the signal reproducibility. Across an investigated gradient from 20 to 60 min (Fig. 5(b)), the RPP exhibited an initial surge followed by saturation as the incubation time extended. At 30 min, target capture in the positive regions approached saturation, and the ARI was maintained at a high level. Further prolonging the reaction to 45–60 min only yielded a marginal increase in absolute signal, but led to a significant deterioration of the non-specific background. To optimally balance detection sensitivity with the signal-to-noise ratio, 30 min was finalized as the optimal immunoassay duration.

Concurrently, the self-assembly quality of 11-MUA on the gold film is the critical determinant of the subsequent capture antibody conjugation density. Comparative results (Fig. 5(c)) indicate that incubation at 4 °C for 24 h significantly outperformed the conditions of 8 h at room temperature and 12 h at 4 °C. Thermodynamic and kinetic analyses suggest that a prolonged, low-temperature environment assists thiol molecules in overcoming the rearrangement energy barrier, facilitating the construction of a highly ordered and continuous monolayer with minimal defects on the gold surface. This densely packed carboxylated interface provides abundant reactive sites for subsequent EDC/NHS activation, drastically enhancing the antibody conjugation efficiency. Consequently, the optimal self-assembly condition for 11-MUA was established as 4 °C for 24 h.

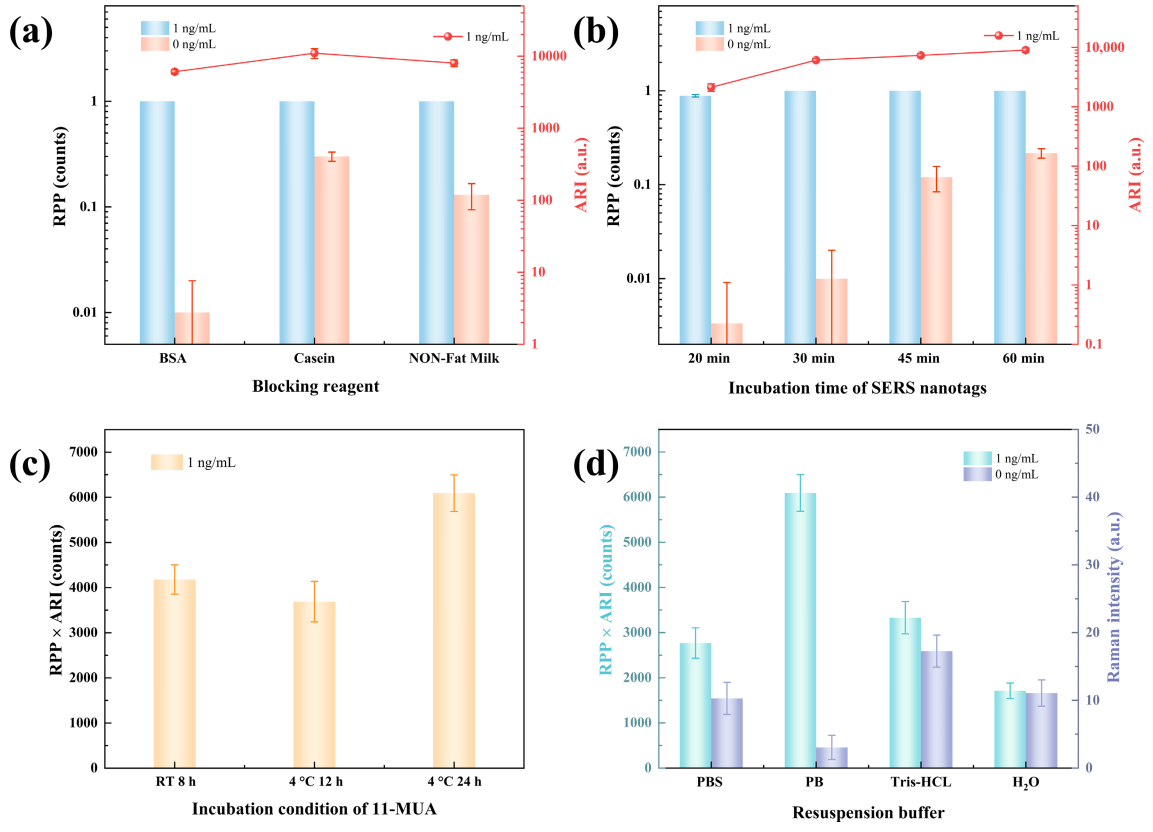

Figure 5 (a) Optimization of surface blocking agents. (b) Optimization of SERS nanotags incubation time. (c) Optimization of the self-assembly conditions for 11-MUA. (d) Optimization of SERS nanotags resuspension buffer.

Finally, the influence of the SERS nanotag resuspension buffer on system performance was investigated. The results demonstrated that the detection signal-to-noise ratio reached its optimum when the PB buffer system was employed (Fig. 5(d)). This is primarily attributed to the positive regulation of protein conformation and binding kinetics by appropriate pH and ionic strength. Specifically, the near-neutral pH effectively maintains the biological activity of the antibody-binding domains, while moderate ionic strength (e.g., via sodium ions) enhances the conformational stability of the antigen-antibody complexes through electrostatic shielding and hydrophobic interactions. Taking all factors into consideration, the PB buffer was selected as the ideal resuspension medium for the SERS nanotags.

3.6 Digital SERS detection of IL-6

In this research, IL-6 was selected as the target model for proof-of-concept validation. As a core cytokine involved in inflammatory and immune responses, IL-6 possesses significant adjunctive value in the early diagnosis of acute infections [37, 38]. Although existing technologies can stably detect IL-6 at levels above ng/mL [39–42], its critical threshold distinguishing the normal physiological baseline from abnormal pathological states in clinical practice is exceedingly low (typically ~ 7 pg/mL) [43]. Furthermore, during the early stages of disease development, its concentration often fluctuates slightly within an ultralow range. Therefore, achieving the accurate and stable detection of IL-6 in the low-concentration regime is of profound clinical significance.

To systematically evaluate the sensitivity performance of the chip, a concentration test gradient ranging from 100 fg/mL to 1 ng/mL was established. Following the completion of the sandwich immunoassay, a 10 × 10 micropillar array region was randomly scanned using a confocal Raman spectrometer. The pseudocolor heat map (Fig. S8 in the ESM), constructed based on the extracted characteristic peak intensity at 592 cm^{-1}, revealed that in the ultralow concentration range (e.g., sub-pg/mL levels), the specific signal of the target gradually diminished and became conflated with background noise. This indicates that the conventional intensity-dependent detection mode faces significant challenges in further enhancing sensitivity. To address this, the pristine Raman matrix was subjected to binarization using the aforementioned statistical threshold (Fig. 6(a)), thereby enabling the precise extraction of positive signals. The results demonstrated that the RPP exhibited a pronounced gradient attenuation as the IL-6 concentration decreased. Within the low-concentration range of 100 fg/mL to 100 pg/mL, the RPP displayed an excellent exponential fitting relationship with the antigen concentration (R^2 = 0.988, Fig. 6(b)). This robustly corroborates that the single-molecule capture events on the micropillar array strictly adhere to Poisson statistics, laying a solid theoretical foundation for the chip as a digital detection platform. To mitigate the signal saturation issue inherent to the single binarization mode at high concentrations (Fig. S9 in the ESM), the binarized image was employed as a spatial mask to perform a convolution operation with the original Raman data. This generated a novel digital heat map integrating both spatial positional information and intensity dimensions (Fig. 6(c)). As depicted in Fig. 6(d), within the range of 100 fg/mL to 1 ng/mL, the RPP × ARI composite metric increased significantly with ascending target concentrations, exhibiting an excellent linear regression relationship with the logarithm of the IL-6 concentration (R^2 = 0.991) (Fig. 6(e)). Compared to the single binarization mode, this

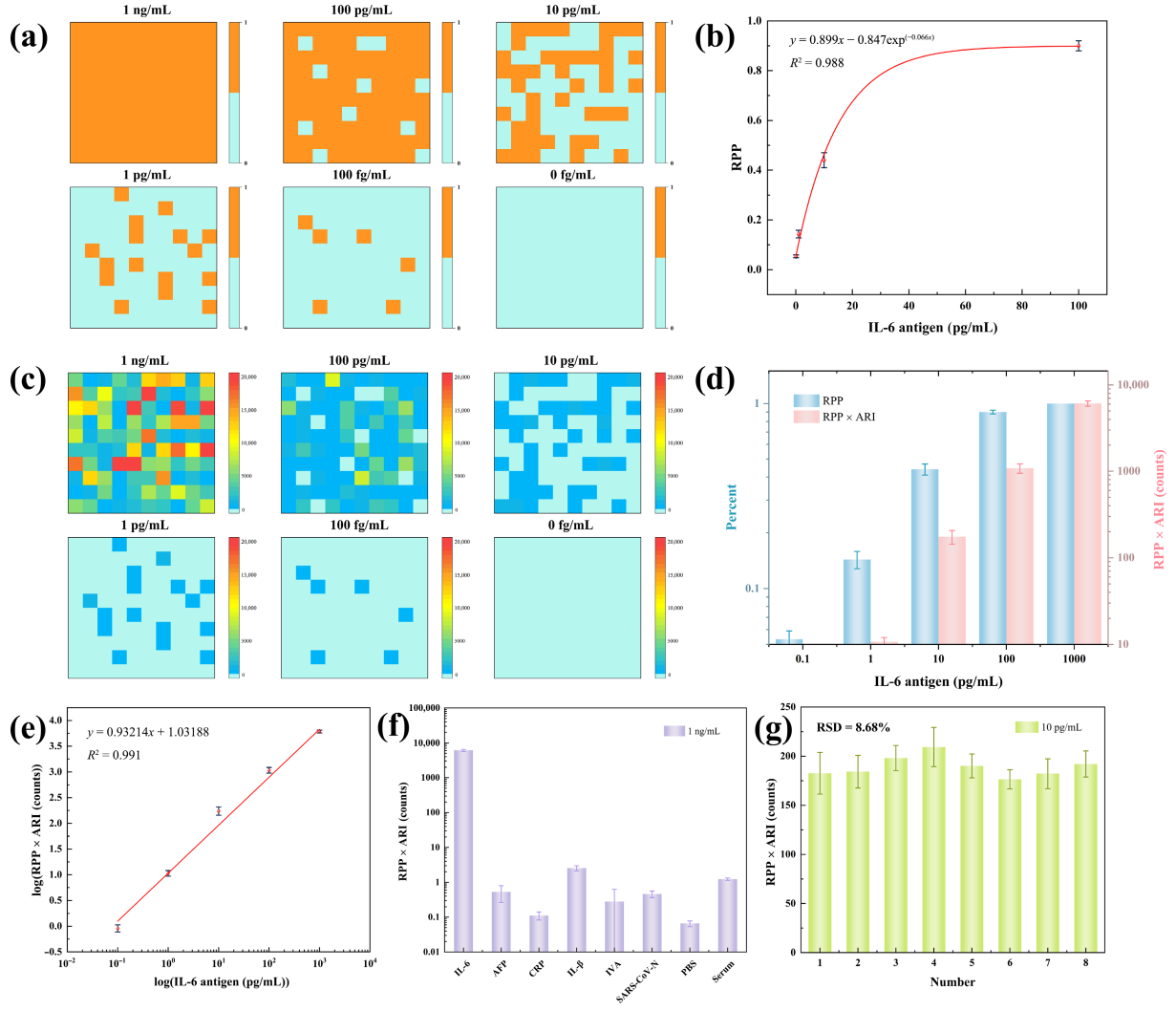

Figure 6 (a) Representative binarized Raman mapping images at various IL-6 concentrations. (b) Exponential fitting curve for the binarization mode. (c) Representative digital SERS mapping images at various IL-6 concentrations. (d) Calculated RPP and RPP × ARI across different concentrations. (e) Linear calibration curve for the digital SERS mode. (f) Specificity evaluation. (g) Reproducibility evaluation.

digital SERS strategy broadened the detection range by 10-fold. Based on the 3σ criterion, the LOD of this system was calculated to be as low as 16.9 fg/mL. A comparative analysis of the proposed gold-capped micropillar array with other reported IL-6 detection methods is summarized in Table S1 in the ESM. Compared with conventional SERS or electrochemical-based detection methods, the proposed digital SERS platform achieves a relatively low LOD, demonstrating its favorable sensitivity for IL-6 detection. Furthermore, specificity validation revealed that a prominent Raman signal was only detected in the presence of the target IL-6, while the signals from the control groups were negligible (Fig. 6(f)), confirming the high selectivity of the substrate. In the reproducibility assessment of the chip, eight parallel experiments were conducted using a 10 pg/mL IL-6 sample. The RSD of the RPP × ARI composite metric was merely 8.68% (Fig. 6(g)), demonstrating the outstanding batch-to-batch reproducibility of the platform.

4 Conclusions

In summary, this research developed a digital sensing platform by plasmonic coupling of SERS nanotags with wafer-scale gold-capped micropillar arrays for the quantitative detection of low-concentration protein biomarkers. Fabricated via high-throughput UVL, the platform combines the physical structural confinement of the substrate with spatially selective chemical modification, and employs a dual-dimensional analysis strategy integrating signal spatial distribution with Raman intensity. Using IL-6 as a validation model, this analytical approach effectively mitigated the signal saturation issue inherent in single binarization counting at high concentrations, achieving a linear dynamic range of 100 fg/mL–1 ng/mL and a LOD of 16.9 fg/mL. This work provides a cost-effective and translational technical solution for the accurate screening of low-abundance biomarkers, and its modular array design lays the foundation for future simultaneous detection of multiple targets on a single chip. Although the sensing feasibility of this platform has been preliminarily demonstrated, advancing it to practical clinical application will require systematic evaluation using large-scale clinical cohorts in future studies.

Electronic Supplementary Material: Supplementary material (materials and equipment, nanotag synthesis, SEM images, SERS spectra, theoretical formulas, and table for performance

comparison) is available in the online version of this article at https://doi.org/10.26599/NR.2026.94909231.

Data availability

All data needed to support the conclusions in the paper are presented in the manuscript and the Electronic Supplementary Material. Additional data related to this paper may be requested from the corresponding author upon request.

Acknowledgements

This work is granted by the National Natural Science Foundation of China (Nos. 82361138570 and 32371393), Shenzhen Science and Technology Program (No. JCYJ20230807114610021), and Urumqi City "Hongshan Sci-Tech Innovation Talents" Small Group Project (No. B241018005).

Declaration of competing interest

All the contributing authors report no conflict of interests in this work.

Author contribution statement

Q. F. Z.: Methodology, investigation, data analysis, writing – original draft. M. M. L.: Methodology, writing – original draft. C. M. Methodology, investigation. Y. L.: Methodology, investigation. J. S.: Investigation. C. C.: Investigation. J. L. S.: Investigation. C. Q.: Validation. Y. H.: Investigation, writing – review & editing. H. Z.: Investigation, writing – review & editing. X. Y. L.: Writing – review & editing. X. W. Z.: Conceptualization, writing – review & editing, supervision, project administration, funding acquisition. All the authors have approved the final manuscript.

Use of AI statement

None.

References

[1] Kim, H.; Hall, D. R.; Nierves, L.; Lin, T. T.; Kitata, R. B.; Shi, T. J.; Liu, T. The evolution of analytical techniques for multiplex analysis of protein biomarkers. *Expert Rev. Proteomics* **2025**, *22*, 255–272.

[2] Li, B. J.; Liu, Y. T.; Kong, L. Y.; Yin, K.; Zhang, P.; Wang, X. Recent advances in single-molecule immunoassays and their clinical applications. *TrAC Trends Anal. Chem.* **2026**, *195*, 118604.

[3] Wu, Y.; Fu, Y. S.; Guo, J. C.; Guo, J. H. Single-molecule immunoassay technology: Recent advances. *Talanta* **2023**, *265*, 124903.

[4] Xu, Y. K.; Aljuhani, W.; Zhang, Y. R.; Ye, Z. W.; Li, C. C.; Bell, S. E. J. A practical approach to quantitative analytical surface-enhanced Raman spectroscopy. *Chem. Soc. Rev.* **2025**, *54*, 62–84.

[5] Yi, J.; You, E. M.; Hu, R.; Wu, D. Y.; Liu, G. K.; Yang, Z. L.; Zhang, H.; Gu, Y.; Wang, Y. H.; Wang, X. et al. Surface-enhanced Raman spectroscopy: A half-century historical perspective. *Chem. Soc. Rev.* **2025**, *54*, 1453–1551.

[6] Nam, W.; Kim, W.; Zhou, W.; You, E. A. A digital SERS sensing platform using 3D nanolaminate plasmonic crystals coupled with Au nanoparticles for accurate quantitative detection of dopamine. *Nanoscale* **2021**, *13*, 17340–17349.

[7] Fan, M. K.; Andrade, G. F. S.; Brolo, A. G. A review on recent advances in the applications of surface-enhanced Raman scattering in analytical chemistry. *Anal. Chim. Acta* **2020**, *1097*, 1–29.

[8] dos Santos, D. P.; Temperini, M. L. A.; Brolo, A. G. Intensity fluctuations in single-molecule surface-enhanced Raman scattering. *Acc. Chem. Res.* **2019**, *52*, 456–464.

[9] Liu, H. R.; Jiang, Z. H.; Hu, Z. W.; Zhang, B. H.; He, T.; Dong, X. H.; Sun, C. W.; Tian, J.; Jiang, W.; Pisanello, F. et al. Spatiotemporal Raman probing of molecular transport in sub-2-nm plasmonic quasi-2D nanochannels. *Sci. Adv.* **2026**, *12*, eaec3641.

[10] Wang, J.; Zhou, Q.; Lowry, K.; Howard, C. B.; Trau, M. Epitope-resolved digital SERS profiling of structurally dynamic antigens via a multi-epitope bispecific antibody framework. *Adv. Sci.* **2026**, *13*, e75828.

[11] Zhang, N.; Liu, Y.; She, X. Y.; Shen, Y.; Tian, X. L.; Jin, C. J. Periodic nanopillar arrays integrated gold-capped silicon nanograsses with nanometer gap for large-area, uniform and sensitive surface-enhanced Raman scattering. *Nano Res.* **2026**, *19*, 94908563.

[12] Liu, H. M.; Lei, Y. A critical review: Recent advances in "digital" biomolecule detection with single copy sensitivity. *Biosens. Bioelectron.* **2021**, *177*, 112901.

[13] Zhang, Y. T.; Gu, H. C.; Xu, H. Recent progress in digital immunoassay: How to achieve ultrasensitive, multiplex and clinical accessible detection. *Sens. Diagn.* **2024**, *3*, 9–27.

[14] Ando, J.; Murai, K.; Michiyuki, T.; Takahashi, I.; Iida, T.; Kogo, Y.; Toyoda, M.; Saito, Y.; Murayama, S.; Kurihara, M. et al. Digital SERS bioanalysis of single- enzyme biomarkers. *Proc. Natl. Acad. Sci. USA* **2025**, *122*, e2510559122.

[15] Bi, X. Y.; Czajkowsky, D. M.; Shao, Z. F.; Ye, J. Digital colloid-enhanced Raman spectroscopy by single-molecule counting. *Nature* **2024**, *628*, 771–775.

[16] Wen, P.; Yang, F.; Zhao, H. X.; Xu, Y.; Li, S. B.; Chen, L. Novel digital SERS-microfluidic chip for rapid and accurate quantification of microorganisms. *Anal. Chem.* **2024**, *96*, 1454–1461.

[17] González-Cabaleiro, L.; Fernández-Lodeiro, C.; Vázquez-Iglesias, L.; Soriano-Maldonado, P.; van Raaij, M. J.; Bodelón, G.; Pérez-Juste, J.; Pastoriza-Santos, I. Pushing the limits of lateral flow immunoassay by digital SERS for the ultralow detection of SARS-CoV-2 virus. *Small Sci.* **2024**, *4*, 2400259.

[18] Liu, X. J.; Zhang, Q. Q.; Zong, C. H.; Gai, H. W. Digital immunoassay for proteins: Theory, methodology, and clinical applications. *Anal. Chem.* **2025**, *97*, 9077–9110.

[19] Shim, J. E.; Kim, Y. J.; Choe, J. H.; Lee, T. G.; You, E. A. Single-nanoparticle-based digital SERS sensing platform for the accurate quantitative detection of SARS-CoV-2. *ACS Appl. Mater. Interfaces* **2022**, *14*, 38459–38470.

[20] Shim, J. E.; Kim, Y. J.; Hahm, E.; Choe, J. H.; Baek, A.; Kim, R. M.; You, E. A. Ultrasensitive SERS nanoprobe-based multiplexed digital sensing platform for the simultaneous quantification of Alzheimer's disease biomarkers. *Biosens. Bioelectron.* **2025**, *274*, 117216.

[21] Miao, X. Z.; Shanmugasundaram, K.; Vedelago, C.; Naei, V. Y.; Kulasinghe, A.; Lobb, R.; Trau, M.; Wuethrich, A. A digital single-molecule nanocavity assay to monitor phosphoprotein circuits in single-cell. *Adv. Mater. Technol.* **2026**, *11*, e02611.

[22] Choi, C.; Kim, H.; Moon, S.; Hwang, I. J.; Choi, S. Y.; Yoon, S.; Hwang, J. H.; Jung, K.; Lee, J. C.; Kim, J. H. Digital SERS nanoprobe immunoassay with single-particle sensing resolution for detection of pancreatic cancer biomarkers from clinical blood samples. *Small Methods* **2026**, *10*, e00005.

[23] Li, J. R.; Sina, A. A. I.; Antaw, F.; Fielding, D.; Möller, A.; Lobb, R.; Wuethrich, A.; Trau, M. Digital decoding of single extracellular vesicle phenotype differentiates early malignant and benign lung lesions. *Adv. Sci.* **2023**, *10*, 2204207.

[24] Li, J. R.; Wuethrich, A.; Sina, A. A. I.; Cheng, H. H.; Wang, Y. L.; Behren, A.; Mainwaring, P. N.; Trau, M. A digital single-molecule nanopillar SERS platform for predicting and monitoring immune toxicities in immunotherapy. *Nat. Commun.* **2021**, *12*, 1087.

[25] Chen, Y. Q.; Bi, K. X.; Wang, Q. J.; Zheng, M. J.; Liu, Q.; Han, Y. X.; Yang, J. B.; Chang, S. L.; Zhang, G. H.; Duan, H. G. Rapid

focused ion beam milling based fabrication of plasmonic nanoparticles and assemblies *via* "sketch and peel" strategy. *ACS Nano* **2016**, *10*, 11228–11236.

[26] Yao, Y.; Cao, L. L.; Sun, X. L.; Wang, Q.; Xu, Z. Y.; Zhai, T. R.; Zhao, Y.; Jiang, Y. J.; Li, Z. G.; Yan, Y. Z. Laser-induced periodic phase-transition of 2D-$MoTe_2$ nanograting template for frequency-shift digital-SERS immunoassay of autoimmune disease. *Adv. Sci.* **2026**, *13*, e75366.

[27] Dupin, A.; Vonshak, O.; Nir, V.; Levanon, M.; Avidan, N.; Divon, Y.; Peleg, S.; Thompson, S.; Noireaux, V.; Daube, S. S. et al. Cell-free immuno-profiling on a genetically programmed biochip. *Nat. Nanotechnol.* **2026**, *21*, 106–115.

[28] Chen, J. N.; Wei, Y. J.; Wang, L. M.; Chen, L. Y.; He, S. N.; Liu, H. L. Digital SERS nanostructured platform for amplification-free single-molecule DNA detection and pre-symptomatic diagnosis of kiwifruit soft rot. *Anal. Chem.* **2025**, *97*, 11317–11327.

[29] Zhu, C. Y.; Lin, X. D.; Jin, R. Y.; Long, C. N.; Zhu, C. N.; Zheng, D. Y.; Yang, X. F.; Zhang, P.; Liu, C. Digital profiling subpopulations of cancer cell-derived exosomes via aptamer-SERS nanotags on a wafer-level micropillar array chip. *ACS Sens.* **2025**, *10*, 6962–6970.

[30] Bido, A. T.; Brolo, A. G. Digital SERS protocol using Au nanoparticle-based extrinsic Raman labels for the determination of SARS-CoV-2 spike protein in saliva samples. *ACS Appl. Nano Mater.* **2023**, *6*, 15426–15436.

[31] Wang, J.; Zhou, Q.; Howard, C. B.; Trau, M. Physicochemical tuning of bispecific antibody fragment immobilization for robust digital SERS biosensing. *Anal. Chem.* **2025**, *97*, 23994–24002.

[32] Wang, M. Y.; Cao, L. L.; Zhang, H. J.; Zhang, C. P.; Sun, X. L.; Yuan, Y. P.; Guo, X. Y.; Guo, X. R.; Zhao, Y.; Jiang, Y. J. et al. Nanohole-in-microsphere array (NiMA): An ultrasensitive digital-SERS tool for serum diagnosis of rheumatoid arthritis. *Biosens. Bioelectron.* **2025**, *287*, 117655.

[33] Wen, P.; Yang, F.; Zhao, H. X.; Li, S. B.; Xu, Y.; Chen, L. Microcavity array-based digital SERS chip for rapid and accurate label-free quantitative detection of live bacteria. *ACS Sens.* **2024**, *9*, 6167–6173.

[34] Lu, Y.; Mo, X. F.; Zhu, G.; Huang, Y.; Wang, Y. C.; Yang, Z. Z.; Gao, L. Q.; Shen, G. F.; Wang, Y.; Zhao, X. W. Ratiometric SERS quantification of SO_2 vapor based on Au@Ag-Au with Raman reporter as internal standard. *J. Hazard. Mater.* **2024**, *467*, 133763.

[35] Lu, Y.; Zhou, Q. F.; Teng, B. Z.; Yang, X.; Huang, Y.; Chen, C.; Lv, X. Y.; Meng, D. H.; Zhao, X. W. Photonic crystal-plasmonic nanoantenna coupling biosensor for AI assisted protein biomarker detection. *Chem. Eng. J.* **2026**, *527*, 171550.

[36] Li, A.; Mo, X. F.; Lu, Y.; Zhu, G.; Liu, C.; Yang, X.; Huang, Y.; Sheng, J. L.; Zhang, H.; Meng, D. H. et al. Digital SERS immunoassay of Interleukin-6 based on Au@Ag-Au nanotags. *Biosens. Bioelectron.* **2025**, *270*, 116973.

[37] Jones, S. A.; Jenkins, B. J. Recent insights into targeting the IL-6 cytokine family in inflammatory diseases and cancer. *Nat. Rev. Immunol.* **2018**, *18*, 773–789.

[38] Zhu, X. Y.; Starosta, S.; Ferrer, M.; Hou, J. X.; Chevy, Q.; Lucantonio, F.; Muñoz-Castañeda, R.; Zhang, F. R.; Zang, K. K.; Zhao, X. et al. A neuroimmune circuit mediates cancer cachexia-associated apathy. *Science* **2025**, *388*, eadm8857.

[39] Chen, R. P.; Du, X.; Cui, Y. J.; Zhang, X. Y.; Ge, Q. Y.; Dong, J.; Zhao, X. W. Vertical flow assay for inflammatory biomarkers based on nanofluidic channel array and SERS nanotags. *Small* **2020**, *16*, 2002801.

[40] Hun, X.; Zhang, Z. J. Functionalized fluorescent core-shell nanoparticles used as a fluorescent labels in fluoroimmunoassay for IL-6. *Biosens. Bioelectron.* **2007**, *22*, 2743–2748.

[41] Zhou, Q. F.; Lu, Y.; Li, M. M.; Qi, C.; Sun, X. X.; Zhang, H.; Sheng, J. L.; Chen, C.; Lv, X. Y.; Zhao, X. W. Self-driven microfluidic chip with integrated lateral and vertical flow assays for dual-readout point-of-care testing. *Biosens. Bioelectron.* **2026**, *294*, 118247.

[42] Zhou, T.; Lu, D. C.; She, Q. T.; Chen, C. R.; Chen, J. B.; Huang, Z. F.; Feng, S. Y.; You, R. Y.; Lu, Y. D. Hypersensitive detection of IL-6 on SERS substrate calibrated by dual model. *Sens. Actuators B: Chem.* **2021**, *336*, 129597.

[43] Miller, E. M.; Mcdade, T. W. A highly sensitive immunoassay for interleukin-6 in dried blood spots. *Am. J. Hum. Biol.* **2012**, *24*, 863–865.

This is an open access article under the terms of the Creative Commons Attribution 4.0 International License (CC BY 4.0, https://creativecommons.org/licenses/by/4.0/).

© The Author(s) 2027. Published by Tsinghua University Press.